

Gravity current flow over sinusoidal topography in a two-layer ambient

Mitchell Nicholson and Morris R. Flynn

Citation: [Physics of Fluids](#) **27**, 096603 (2015); doi: 10.1063/1.4931120

View online: <http://dx.doi.org/10.1063/1.4931120>

View Table of Contents: <http://scitation.aip.org/content/aip/journal/pof2/27/9?ver=pdfcov>

Published by the [AIP Publishing](#)

Articles you may be interested in

[Global chaotization of fluid particle trajectories in a sheared two-layer two-vortex flow](#)

[Chaos](#) **25**, 103108 (2015); 10.1063/1.4930897

[Influence of an external force field on the dynamics of a free core and fluid in a rotating spherical cavity](#)

[Phys. Fluids](#) **27**, 074106 (2015); 10.1063/1.4926804

[Influence of Prandtl number on the instability of natural convection flows within a square enclosure containing an embedded heated cylinder at moderate Rayleigh number](#)

[Phys. Fluids](#) **27**, 013603 (2015); 10.1063/1.4906181

[Modification of quasi-streamwise vortical structure in a drag-reduced turbulent channel flow with spanwise wall oscillation](#)

[Phys. Fluids](#) **26**, 085109 (2014); 10.1063/1.4893903

[Reducing the data: Analysis of the role of vascular geometry on blood flow patterns in curved vessels](#)

[Phys. Fluids](#) **24**, 031902 (2012); 10.1063/1.3694526

Did your publisher get
18 MILLION DOWNLOADS in 2014?

AIP Publishing did.



THERE'S POWER IN NUMBERS. Reach the world with AIP Publishing.



Gravity current flow over sinusoidal topography in a two-layer ambient

Mitchell Nicholson and Morris R. Flynn

Department of Mechanical Engineering and Institute for Geophysical Research, University of Alberta, Edmonton, Alberta T6G 2G8, Canada

(Received 21 January 2015; accepted 5 September 2015; published online 23 September 2015)

We report upon a laboratory experimental study of dense full- and partial-depth locks released gravity currents propagating through a two-layer ambient and over sinusoidal topography of amplitude A and wavelength λ . Attention is restricted to a Boussinesq flow regime and the initial (or slumping) stage of motion. Because of the presence of the topography, the lower layer depth and channel depth vary in the downstream direction by as much as $\pm 52\%$ and $\pm 40\%$, respectively. Despite such large variations, the instantaneous gravity current front speed typically changes by only a small amount from its average value, \bar{U} . We conclude that the reason for this unexpected observation is a counterbalancing between the contraction/expansion of the channel on one hand and along-slope variations of the buoyancy force on the other hand. Compared to the case of gravity current flow over a horizontal surface, the topography has a retarding effect on \bar{U} ; we characterize the variation of \bar{U} with the following parameters: A , A/λ , the interface height, the height of gravity current fluid inside the lock, and the layer densities as characterized by $S \equiv (\rho_1 - \rho_2)/(\rho_0 - \rho_2)$ where ρ_0 is the gravity current density, ρ_1 is the lower ambient layer density, and ρ_2 is the upper ambient layer density. The topography also alters the structure of the gravity current head by inducing large-scale Kelvin-Helmholtz (K-H) vortices directly downstream of regions of significant shear. These vortices are transient flow features; after formation and saturation, they relax at which point gravity current fluid sloshes back and forth in the topographic troughs. A simple geometric model is presented that prescribes the minimum number of topographic peaks a gravity current fluid will overcome. As in the horizontal bottom case, the forward advance of the gravity current can excite a downstream-propagating interfacial disturbance, which is more prominent for larger S . We identify when the gravity current front will travel faster (supercritical flow) or slower (subcritical flow) than the interfacial disturbance based on S and A/λ . Unlike in the horizontal-bottom case, however, we typically also observe interfacial oscillations far ahead of the gravity current front. These have wavelength approximately equal to λ and are due to spatial variations in the speed of the ambient return flow. © 2015 AIP Publishing LLC. [<http://dx.doi.org/10.1063/1.4931120>]

I. INTRODUCTION

Gravity currents occur naturally in situations where there is a horizontal difference of density between two fluids. They are ubiquitous in nature and appear as avalanches, dust storms, micro-bursts, sea breezes, and pollutant spills, among many other examples outlined by Simpson.¹ The study of gravity currents is important for understanding how buoyancy-driven flow in nature or industry might impact human populations, ecosystems, and agricultural production.

After the seminal analysis of Benjamin,² many studies examined gravity current flow over a horizontal surface in a uniform ambient. A complication associated with natural flow is that the bottom boundary is rarely horizontal. Two-layer and continuously stratified flow over topography has consequences for momentum transport in the atmosphere and oceans and has been extensively researched in case of unidirectional flow by Castro *et al.*,³ Snyder *et al.*,⁴ Hunt *et al.*,⁵ Castro and Snyder,^{6,7} Baines,⁸ and Belcher and Hunt.⁹ This body of the literature was expanded upon

by Armi,¹⁰ Farmer and Armi,¹¹ Dalziel and Lane-Serff,¹² and Baines⁸ who considered steady exchange flows over sills or through lateral contractions. Gravity current flow over topography shares some similarities with the two-layer exchange flow problem; an important difference, however, is that gravity currents, particularly those generated by lock-release, evolve in time and so are not amenable to steady analysis except just behind the front where the flow can become quasi-steady. There are, in other words, numerous interesting transient flow features to be considered such as the downstream propagation of the gravity current front and the excitation of Kelvin-Helmholtz billows and of interfacial waves.

Many of these transient features have been described by Peters and Venart,¹³ La Rocca *et al.*,¹⁴ and Nogueira *et al.*¹⁵ who studied gravity current flow over a rough bed and by Lane-Serff *et al.*,¹⁶ Özgökmen *et al.*,¹⁷ Gonzalez-Juez *et al.*,¹⁸ and Tokyay *et al.*^{19,20} who examined the influence of larger-scale topography. Relative to the horizontal bottom case, these studies found that topographic features, whether large or small, can alter the gravity current structure and can exert a drag that reduces the gravity current front speed. Most notably, perhaps, Tokyay *et al.*¹⁹ determined by way of detailed numerical simulations that the magnitude of the drag force depends largely on the obstacle shape; comparatively blunt objects exhibit a more significant drag.

The studies cited in the previous paragraph consider an ambient that is uniform in density. The flow dynamics are expected to be more complicated if this assumption is relaxed as may be appropriate when the gravity current and topographic heights are comparable to the vertical scale over which ambient density changes are appreciable. Examples include an outflow or sea-breeze front propagating over a set of hills and beneath an atmospheric inversion, or the accidental release of a dense pollutant onto an undulating lake bed where the lake water supports a strong thermocline. Of course, gravity current flow through density-stratified media is a fertile research topic even in the absence of topographic elements. The past dozen years have seen the publication of studies that have explored the influence of density-stratification be it linear (Maxworthy *et al.*,²¹ Ungarish,^{22,23} two-layer (Tan,²⁴ Flynn, Ungarish and Tan,²⁵ White and Helfrich,²⁶ Sahuri *et al.*²⁷) or otherwise (White and Helfrich²⁸). The general consensus is that ambient stratification admits richer flow dynamics because the gravity current can be non-trivially influenced by the internal waves generated by the collapse and forward advance of dense gravity current fluid. This effect is particularly striking when the front speed is less than the wave speed. In this “subcritical” case, illustrated in figures 6 and 12 of Tan *et al.*,²⁹ for instance, the wave overtakes the gravity current leading to an abrupt deceleration of the front, whose subsequent downstream propagation is typically irregular in time.

Synthesizing the disparate scenarios described above, the objective of the present contribution is to study the flow of a gravity current over topography in a two-layer ambient using laboratory experiments (Figure 1). Because the parameter space associated with our (lock-release) laboratory experiments is potentially quite broad, we restrict attention to Boussinesq flows where density differences are below 10%. Moreover, and so as to further differentiate our study from that of Tokyay *et al.*,¹⁹ we consider sinusoidal topography rather than their repeating pattern of rectangular “ribs” or asymmetric dunes. In this capacity and considering the relative lack of previous

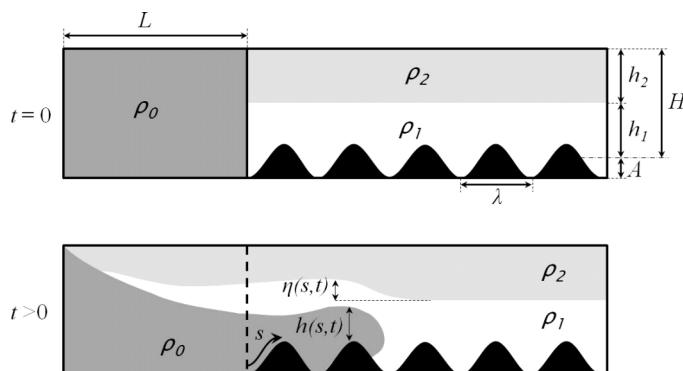


FIG. 1. Schematic of a gravity current flowing over topography in a two-layer ambient.

experimentation in this area, sinusoidal topography is a sensible starting point given its symmetry and lack of sharp corners so that the flow is not unduly influenced by flow separation effects. Our topography has amplitude A , wavelength λ , and mean absolute slope $4A/\lambda$. As we shall illustrate below, it is this latter parameter, in particular, that exerts a significant influence on the qualitative and quantitative features of the flow. Also important, of course, are the ratios of the topographic amplitude, A , lower layer depth, h_1 , and initial lock-fluid depth, D , to the mean channel depth, H . Our experiments span the range $0.1 \leq A/H \leq 0.4$ and are therefore quite different from those investigations that consider gravity current flow either along a rough-bed (Nogueira *et al.*¹⁵), up an infinite slope (Bonnetaze and Lister,³⁰ Marleau *et al.*³¹), or down an incline (Britter and Linden,³² Alavian *et al.*,³³ Monaghan *et al.*,³⁴ and Baines³⁵).

Note finally that gravity currents produced by lock exchange and propagating over a horizontal surface in a uniform ambient typically evolve through a series of sequential phases (Rottman and Simpson³⁶). The first of these is the slumping phase where the front speed is constant. Thereafter, the flow evolves in a self-similar fashion; the front position, x_N , varies with time as $x_N \sim t^{2/3}$ then later, once viscosity becomes important, as $x_N \sim t^{1/5}$. In the present inquiry, gravity current fluid may become isolated in topographic troughs and therefore scaling relationships of Rottman and Simpson do not necessarily apply. Indeed, in the study by Tokyay *et al.*,¹⁹ the periodic array of square ribs on the bottom boundary results in an additional drag-dominated regime, which occurs after the initial slumping phase and is characterized by $x_N \sim t^{0.72}$. For still larger topography of the type considered here, the isolation of gravity current fluid in adjacent troughs leads, in some cases, to instances where the front comes to nearly a complete stop whilst flowing upslope. Part of the present focus is to determine whether and how those factors responsible for this sudden deceleration (factors such as topography and, to a lesser extent, internal waves) modify the front speed measured at comparatively early times. In obvious contrast to the horizontal bottom case, these experimental measurements of the initial front speed show local variations as the front propagates either up- or downslope. However, a surprising observation stemming from our laboratory data is that the variations are very often small in magnitude. Thus, the average initial front speed, \bar{U} , typically does not exhibit a systematic variation over a horizontal distance spanning several topographic features, even for large A . A possible explanation for this unexpected experimental finding is presented and discussed below.

The rest of the manuscript is organized as follows: In Section II, we describe the experimental setup with details of the experimental video post-processing provided in Section II B. Thereafter, Section III describes qualitative and quantitative data from the laboratory. Finally, Section IV presents a series of conclusions and also identifies topics for future investigation.

II. EXPERIMENTS

A. Equipment and experimental procedure

Experiments were performed in a 225.0 cm long by 25.0 cm wide by 30.0 cm tall glass tank which was uniformly backlit using an electric vinyl light sheet. Topography was cut from blue closed-cell styrofoam using a hot wire guided by sinusoidal wooden forms that were fabricated with the aid of a band-saw. In order to avoid the complications associated with securing foam topography to the bottom of the tank, the topography was instead inverted, levelled, and secured, with the help of steel weights and C-clamps, along the free surface. Experiments were therefore run upside-down relative to the schematic of Figure 1. Such a change of orientation does not alter the fundamental dynamics of the flow provided that density contrasts are modest so that the system is Boussinesq, which is the case here. Given this equivalence, and to be consistent with our earlier discussion, results will be presented and described assuming a bottom-propagating gravity current as illustrated in Figure 1. We can assume that the free surface, where it is present, acts as a rigid lid because the flow speeds within each experiment are much less than the free-surface gravity wave speed, \sqrt{gH} (Baines⁸).

To achieve the different densities required for each experiment, salt was mixed with fresh water and dye (food colouring) was added for flow visualization purposes. The density, ρ_0 , of the lock

fluid (dyed red) and the density, ρ_2 , of the lower layer (dyed blue) were in all cases set to the approximate values of 0.998 g/ml and 1.055 g/ml, respectively. This left ρ_1 , the density of the clear upper layer, to dictate the value of the density ratio, $S \equiv (\rho_1 - \rho_2)/(\rho_0 - \rho_2)$, which is used to characterize the density differences between the fluid layers. Densities were, in all cases, measured to within ± 0.00001 g/ml using an Anton Paar DMA 4500 density meter.

1. Full-depth lock release experiments

To prepare the two-layer ambient, a layer of fresh water was first added to the tank to a depth of $h_{1,0}$. Granulated salt was then manually mixed into this fluid until its density reached a value of ρ_1 . Once the salt was completely dissolved, residual turbulent motions were allowed to dissipate for 2 min before blue fluid of density ρ_2 was pumped underneath the clear layer using a Little Giant 3-MD centrifugal pump. In order to decrease the speed of the incoming fluid and to maintain well-mixed conditions in the reservoir containing fluid of density ρ_2 , most of the fluid discharged by the pump was recycled to the supply reservoir using a return line controlled by ball valves. Moreover, the dense blue fluid was pumped through a sponge diffuser located along the bottom of the tank which minimized mixing between the two ambient layers. What mixing did occur was characterized by measuring the thickness of the interface between the upper and lower layers using a MSCTI conductivity probe (Precision Measurement and Engineering) connected to a Velmex stepper motor and controlled using LabVIEW software. The interface thickness was typically less than 2.0 cm, whereas H , the average channel depth, ranged from 10.2 cm to 18.0 cm. In any event, figure 10 of Tan *et al.*²⁹ suggests that the interface thickness has only a minor impact on the front speed, at least in the case of gravity current flow over a horizontal boundary. The height, h_1 , of the top clear layer was defined as the vertical distance from the ambient interface to the mean elevation of topography—see Figure 2. Note that h_1 was either equal to, three times, or one-third of h_2 , the depth of the lower ambient layer.

The fresh water lock-region was created by closing the lock gate at a horizontal distance of 48.7 cm from the left side of the tank and cycling in fresh tap water from above while simultaneously draining progressively more diluted lock fluid from a through-wall fitting and valve located on the bottom surface of the tank. Fresh water cycling occurred over a period of 15 min after which the valve was closed and the lock fluid was dyed red by addition of 3 ml of red food colouring. In total, filling the tank using the above procedure took between 3 and 4 h depending on the value of h_2 . Three sinusoidal topographic profiles were used having the following combinations of amplitude, A , and wavelength, λ : $A = 2.0$ cm and $\lambda = 24.0$ cm; $A = 4.0$ cm and $\lambda = 24.0$ cm; and finally, $A = 4.0$ cm and $\lambda = 48.0$ cm. By varying H , A/H values of 0.11, 0.25, and 0.39 were realized when $A/\lambda = 0.083$. Likewise $A/H = 0.25$ and 0.39 when $A/\lambda = 0.167$. For $A/H \lesssim 0.1$, the flow resembles a gravity current propagating over a (very) rough bed, cf. Nogueira *et al.*¹⁵ Conversely, for $A/H \gtrsim 0.4$, the flow resembles, locally, a gravity current propagating up or down a constant slope, problems that have, respectively, been investigated by, for example, Marleau *et al.*³¹ and Bonnacaze and Lister.³⁰

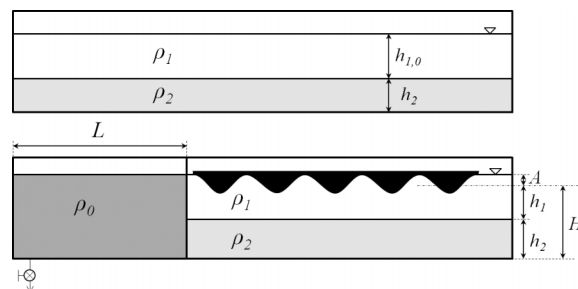


FIG. 2. Schematic illustrating the tank filling process for a representative inverted full-depth lock release experiment. Note that $h_1 = h_{1,0} - A + V_{\text{sub}}/A_o$ where V_{sub} is the volume of the topography below the free surface and A_o is the plan area of the tank (including the lock and ambient regions).

2. Partial-depth lock release experiments

With the inclusion of D/H , the parameter space associated with varying all of the above variables becomes very large. For the experiments described in this subsection, therefore, we restrict attention to ambient interface heights described by $h_1/H = 0.5$. A full factorial batch of experiments was run to characterize the flow dynamics associated with varying not only the topography but also S (six values between 0 and 1) and D/H (three values, i.e., 0.5, 0.75, and 1.0).

To create the fluid layers, the tank was first filled with fresh water to a height of

$$h_{1,0} = \frac{H}{2} + A - \frac{V_{\text{sub}}}{A_c}, \quad (1)$$

where A_c is the planar area of the ambient region of the tank and V_{sub} is the volume of the topography below the free surface. Next, the lock gate was closed and salt was mixed into the ambient-side fluid until the target density of ρ_1 was achieved. Fresh water and approximately 3 ml of red dye were then added to the lock-region to a height of $h_0 = D + A$.

A ~ 50 l batch of blue dyed fluid having a density of $\rho_2 = 1.055$ g/ml was then mixed in a separate container. Using the same setup as described in Section II A 1, this blue dyed fluid was added very slowly outside of the lock to create a sharp interface between the upper and lower ambient layers. Once the free surface outside of the lock was approximately 1 cm above the free surface inside of the lock, the hose was moved to the lock-side of the gate. Fluid addition continued until the lock fluid depth exceeded the ambient fluid depth by an amount $h_0 - h_{1,0} - \frac{1}{\rho_2}(h_0\rho_0 - h_{1,0}\rho_1)$. At this point, the two sides were approximately hydrostatically balanced and the lock gate was opened very slightly to introduce a 0.3 cm gap along the base of the channel—see the upper panel of Figure 3. The tank was then filled with blue fluid of density ρ_2 to a terminal depth of $H + A - V_{\text{sub}}/A_c$. Finally, the topography was very slowly lowered into the ambient-side of the tank and secured at the free surface with the gate still slightly open.

The lower panel of Figure 3 shows the experimental initial conditions once the gate was subsequently closed. During this approximately 3 h filling process, we recorded the values of h_0 , $h_{1,0}$, and the free surface heights on both sides of the gate with and without the topography.

B. Recording and post-processing of laboratory images

Experiments were recorded using a Canon Rebel EOS Rebel T3i camera. To minimize parallax errors, the camera was placed 3.75 m from the front of the tank. The CCD chip was located 1.35 m above the ground, coinciding with the approximate mid-depth of the channel. Note finally that the camera was positioned so that it pointed perpendicular to the middle of the topography. Experimental movies were trimmed, cropped, stripped of audio, and reduced from the default 24 fps variable frame rate to a 12 fps constant frame rate using Avidemux software.

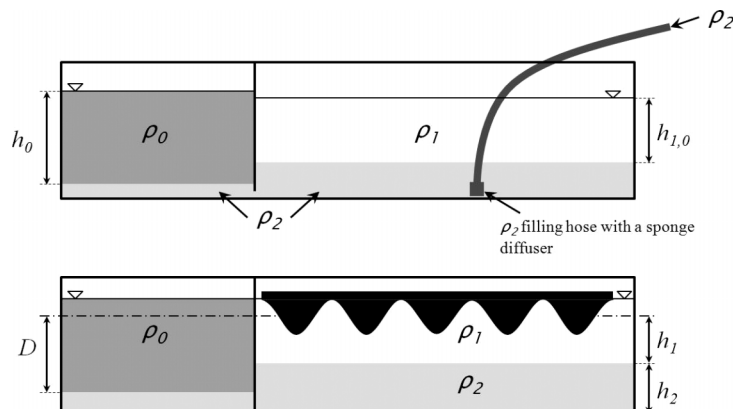


FIG. 3. Schematic illustrating the filling process for a representative inverted partial-depth lock release experiment.

All experimental images are analyzed “upside down” so as to be consistent with the orientation suggested in Figure 1 and the discussion of Section I. Correspondingly, the description of the experimental images and results will presume topographic elements placed along the bottom, not the top, of the channel. Post-processing of laboratory images was performed using a Matlab algorithm that exploited changes of pixel intensity to determine the gravity current height, h , as a function of time, t , and curvilinear position, s , which is defined in Figure 1. The algorithm was based on (3.1) and (3.2) from Shin *et al.*³⁷ and determines the gravity current height using the depth-averaged blue component pixel intensity, devoid of subjective input on the part of the experimenter. Restricting attention to the blue component allows the algorithm to interpret the two ambient layers as a single uniform layer. Thus, for each column of pixels falling between the far left- and right-hand sides of the topography, a vertical time-series (VTS) was created. The algorithm thereby determined, as a function of time, the gravity current height in horizontal increments of approximately 0.11 cm between $x = 0.0$ cm and $x = 119.0$ cm for $\lambda = 24.0$ cm and between $x = 0.0$ cm and $x = 95.8$ cm for $\lambda = 48.0$ cm. Finally, by combining data from all VTS images, composite time-series (CTS) figures showing h/H as a function of t^* and s/L were constructed (see Figure 4 below). Here L is the lock-length and t^* is defined as

$$t^* \equiv \frac{t}{H} \sqrt{g'_{02} H}, \tag{2}$$

where g'_{02} is the reduced gravity of the system defined by

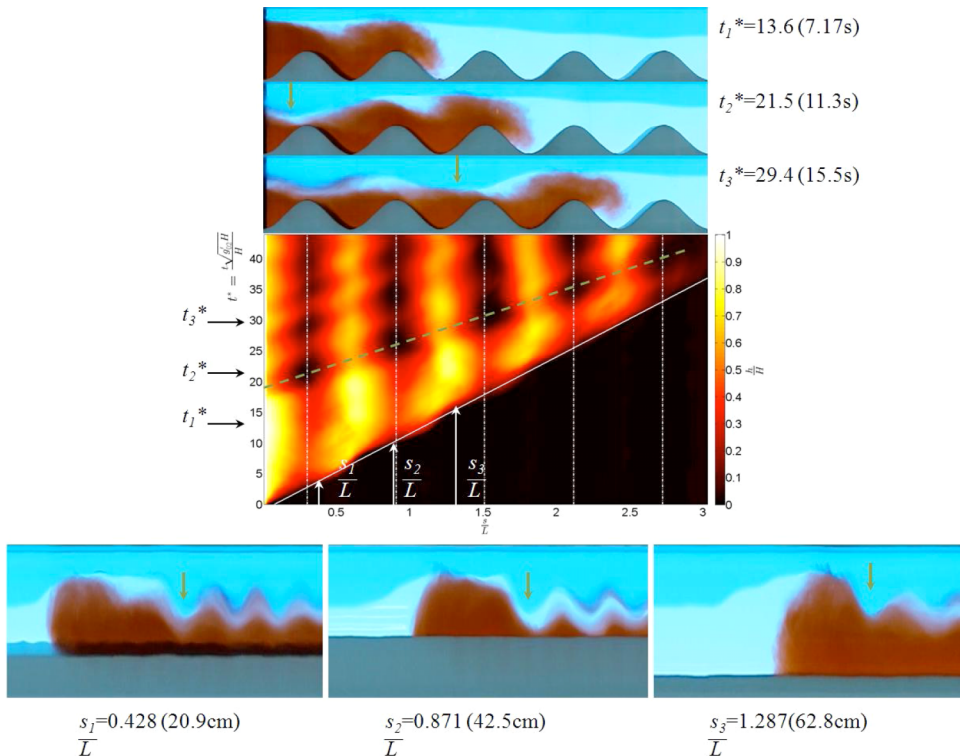


FIG. 4. Above, three snapshots of an experiment are shown at times $t_1^* = 13.6$, $t_2^* = 21.5$, and $t_3^* = 29.4$. These snapshot images have horizontal and vertical axis limits of $0.0 \text{ cm} \leq x \leq 119.0 \text{ cm}$ and $0.0 \text{ cm} \leq z \leq 22.2 \text{ cm}$, respectively, and are aligned with the composite time-series (CTS) shown in the middle where vertical dashed lines indicate the curvilinear location of the topographic peaks. The times t_1^* , t_2^* , and t_3^* are indicated by the black horizontal arrows. Below, three vertical time-series (VTS) that have horizontal and vertical axis limits of $0.0 \text{ s} \leq t \leq 23.3 \text{ s}$ and $0.0 \text{ cm} \leq z \leq 22.2 \text{ cm}$, respectively, and are shown at curvilinear positions $s_1/L = 0.428$, $s_2/L = 0.871$, and $s_3/L = 1.287$. These locations are indicated by the white vertical arrows. The green arrows and green dashed line indicate the position of the ambient reflected wave. Below the green dashed line is a diagonal white line whose slope specifies \bar{U} , the average initial front speed. Note that the dark band just above the topography in the left-hand VTS is a result of parallax where the far side of the topography is visible to the camera. Experimental parameters are as follows: $S = 0.732$, $D/H = 1.0$, $A/H = 0.242$, $A/\lambda = 0.167$, and $h_1/H = 0.509$.

$$g'_{02} \equiv g \frac{|\rho_0 - \rho_2|}{\rho_0}. \quad (3)$$

Examples of three different VTS are shown in the bottom of Figure 4; above these is the corresponding CTS image. The gravity current appears to be orientated “backwards” in the VTS because, with t being the horizontal axis variable, no gravity current fluid reaches the prescribed column of pixels until a certain time, dependent on the downstream location of the column of pixels relative to the lock gate, has elapsed.

From each CTS, the gravity current front position could easily be located. It was therefore possible to estimate a Froude number, $Fr = \bar{U} / \sqrt{g'_{02} H}$, based on \bar{U} , the average initial front speed, which was found from the slope of the best fit line applied to those CTS data giving the (curvilinear) position of the front vs. t . When $\lambda = 24.0$ cm, the CTS data in question fell between the first and the third topographic peaks, except when the front did not propagate all the way to the third peak. In this case, and also when $\lambda = 48.0$ cm, the CTS data in question fell between peaks one and two. These intervals were specially selected to include up- and downslope segments of equal length and also guaranteed that the gravity current remained in the slumping phase, regardless of the experimental parameters.

The forward advance of the gravity current resulted in an ambient return flow in the form of a gravity current of fluid of density ρ_2 that flowed into the lock. When this gravity current reached the lock end-wall, it was reflected as an ambient reflected wave, which propagated downstream at a speed faster than \bar{U} . Figure 4 shows the position of the first trough of this ambient reflected wave with the green vertical arrows; these appear in both the snapshot and the VTS images. The curvilinear position of the first trough of the ambient reflected wave is indicated in the CTS by the green dashed line. In the case of Figure 4, and all the experiments described hereafter, the ambient reflected wave did not directly impact the reported Froude number because the wave did not overtake the gravity current front within the bounds in which Fr was measured. Nonetheless, it was possible, to estimate whether the gravity current represented a supercritical or subcritical flow based on a comparison between the front speed and the speed of the interfacial disturbance excited by the forward advance of the gravity current. To estimate the interfacial disturbance speed, we first constructed CTS images showing the normalized displacement, η/H , of the ambient interface—see Figure 5. The light band that runs from the bottom left to top right corresponds to the interfacial

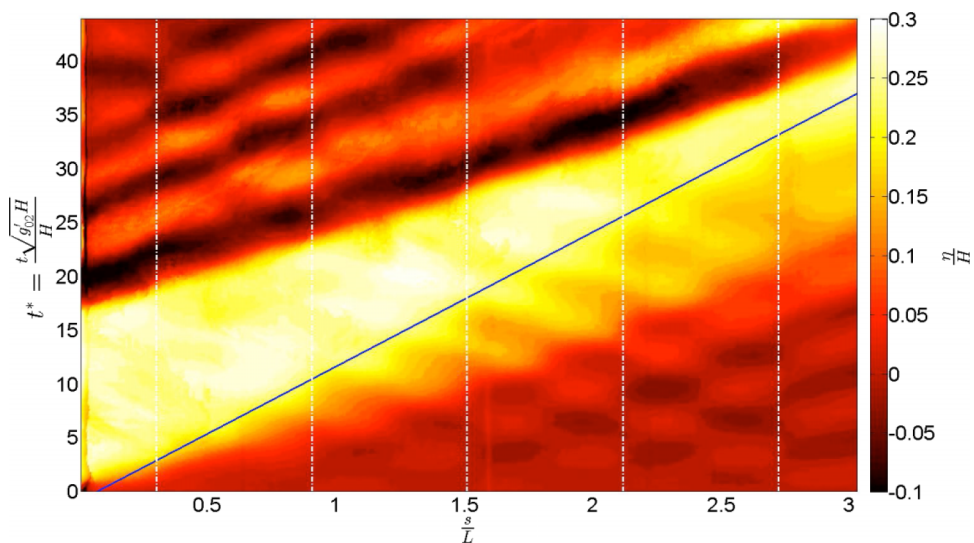


FIG. 5. CTS showing η/H for the same experiment as Figure 4. The solid line is extracted from Figure 4 and shows the average position of the gravity current front. Ahead (bottom right side of the solid line) and behind (top left side of the solid line) the front, interfacial motions are plainly evident. The bright band corresponds to the interfacial disturbance and the dark bands behind the front correspond to the first, second, third, and fourth troughs of the ambient reflected wave.

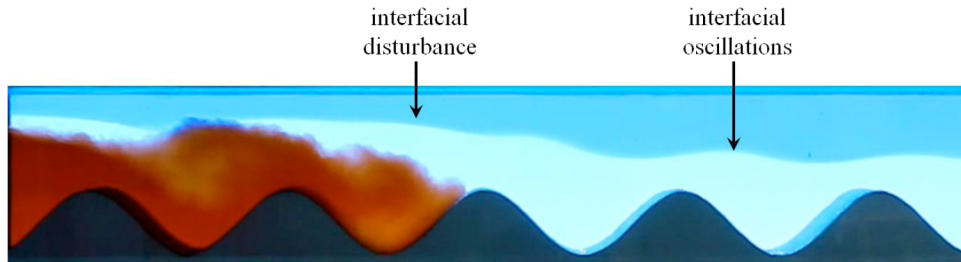


FIG. 6. Experimental snapshot at $t^* = 13.3$ showing an interfacial disturbance, which is due to the forward advance of the gravity current, and downstream oscillations, which are due to spatial variations in the ambient return flow. The above frame measures 115 cm long by 20.7 cm tall and experimental parameters are as follows: $S = 0.534$, $D/H = 1.0$, $A/\lambda = 0.167$, $A/H = 0.242$, and $h_1/H = 0.504$.

disturbance that lay above the gravity current head. Because the speed of this interfacial disturbance was larger than that of the front, the gravity current shown in Figures 4 and 5 was of subcritical type. After the light band in Figure 5 is a dark-coloured band that corresponds to the first trough of the ambient reflected wave and which appears when $t^* \approx 18$ as anticipated by the green dashed line of Figure 4. (Further discussion of sub- vs. supercritical flow is provided in Section III B below.)

CTS images such as Figure 5 are valuable because they also reveal vertical deflections to the ambient interface well ahead of the gravity current front. Attention is here focused on the region below and to the right of the light band where a “checkerboard” pattern having wavelength λ can be seen. As confirmed by Figure 5 and, more especially, Figure 6, these downstream disturbances are of comparatively small amplitude. They arise because the bottom boundary is corrugated. Consequently the ambient return flow is spatially variable rather than uniform. The downstream disturbances are not dispersive waves that detach from, and propagate ahead of, the interfacial disturbance because the downstream disturbances arise at the far end of the tank immediately after the lock gate is withdrawn—see the lower right-hand corner of Figure 5.

III. RESULTS

A. Front speed (full- and partial-depth lock release gravity currents)

Figure 7 shows Fr for the full-depth lock release gravity currents vs. the density ratio, S , for different values of h_1/H , A/H , and A/λ . The data from Figure 7 consist of 30 two-layer, flat-bottom experiments from the work of Tan *et al.*²⁹ combined with 54 two-layer experiments with topography included. Note that Figure 7(a) with $h_1/H \approx 0.25$ contains fewer data points than does Figure 7(c) with $h_1/H \approx 0.75$ because of the requirement that the ambient interface must lie strictly above the topographic peaks.

For both experimental data sets, Fr decreases as S increases. This behavior becomes more pronounced for larger h_1/H : as the lower layer depth increases, the depth-weighted mean density decreases and the driving force for motion (which depends on the difference of density between the gravity current and the ambient) diminishes. The forcing imparted by the topography also acts to decrease Fr . Note, however, that data points having the same value of A/λ cluster to a greater extent than do data points with the same value of A/H , even for A/H as large as 0.4. In other words, for the undulating topography of interest here, it is the topographic slope rather than the topographic amplitude that plays the more substantial role in setting the front speed. This assertion is confirmed by Figure 8; it indicates that Fr changes very little as a function of A/H when all other experimental parameters are held constant. Consistent with the above statement, Tokyay *et al.*¹⁹ suggest that the form drag of a bottom surface obstacle depends on its “degree of bluntness” which, for the sinusoidal topography of interest here, is encapsulated by A/λ .

Similar results to Figure 7 are observed in the case of our 36 partial-depth lock release experiments. In particular, Figure 9 presents data having various D/H but fixed ambient interface height, i.e., $h_1/H = 0.5$. More specifically, the figure shows the variation of Fr with S for three different

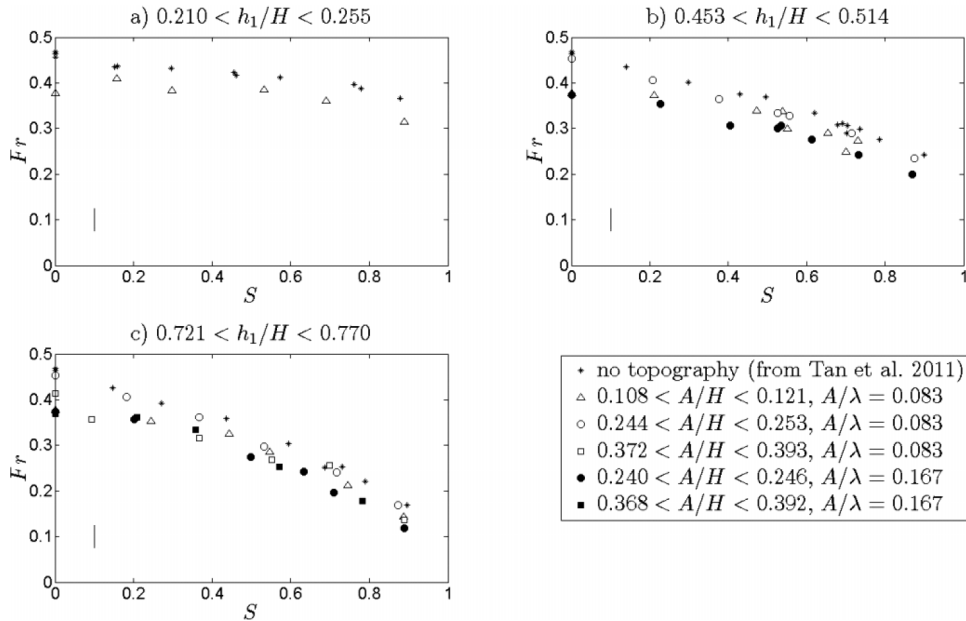


FIG. 7. Variation of Fr with S for various h_1/H , A/H , and A/λ . Representative error bars based on the results of repeat experiments are as indicated in the bottom-left corner of each panel. Error bars in the horizontal direction are comparable to the width of the vertical error bar.

topographic profiles. In contrast to Figure 7 where data are divided into panels based on h_1/H , Figure 9 separates data based on topographic profile in order to isolate the effect of changing D/H . For reference purposes, we also include in Figure 9 data from 15 full-depth lock release experiments drawn from the study of Tan *et al.*²⁹ where no topography is present. Changing D/H does not alter the qualitative relationship between Fr and S : as with the data sets of Figure 7, those of Figure 9 indicate that Fr and S are inversely related whether D/H is comparatively large or

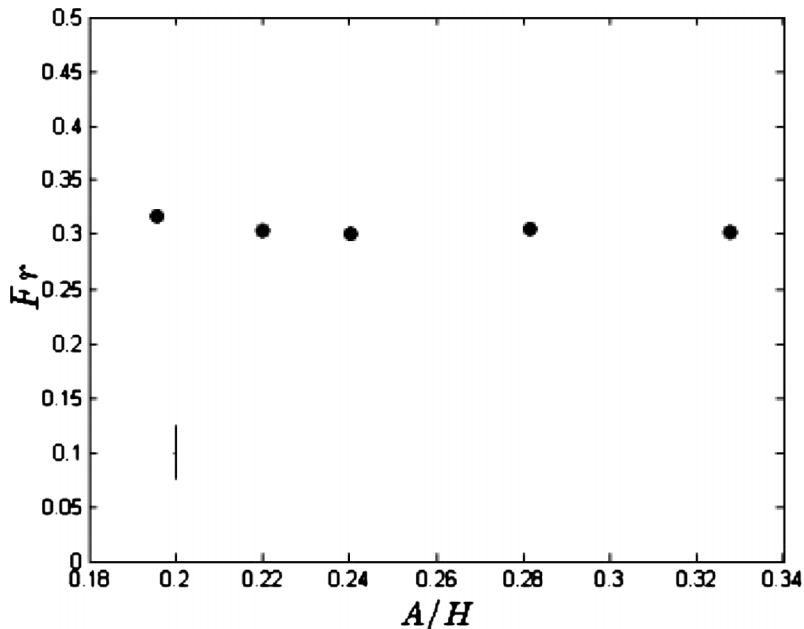


FIG. 8. Variation of Fr with A/H for fixed values of A/λ ($A/\lambda = 0.167$), h_1/H ($0.49 < h_1/H < 0.51$), and S ($0.51 < S < 0.53$). A representative error bar based on the results of repeat experiments is indicated in the bottom-left corner of the figure.

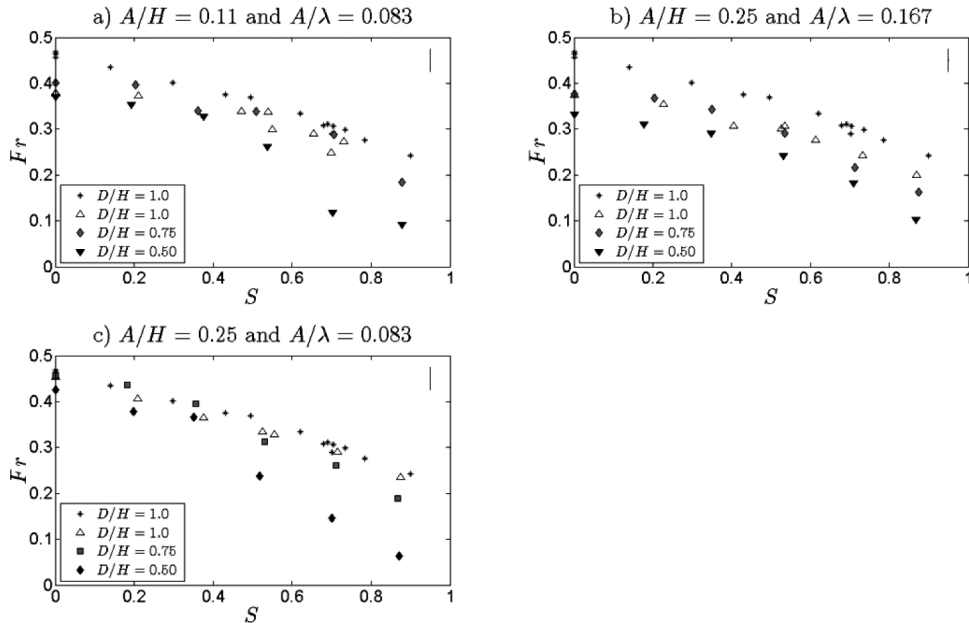


FIG. 9. Variation of Fr with S for various A/H , A/λ , and D/H . Representative error bars based on the results of repeat experiments are as indicated in the top-right corner of each panel. Error bars in the horizontal direction are comparable to the width of the vertical error bar. The starred $D/H = 1.0$ data shown above correspond to cases without topography and are drawn from the study of Tan *et al.*²⁹

small. Note, however, that when topography is present, the $D/H = 1.0$ and $D/H = 0.75$ data sets are almost indistinguishable, particularly for small and moderate S , whereas the $D/H = 0.5$ data show a consistently smaller value for the front speed. Insights into this observation are obtained from Figure 10, which shows, for different S and D/H , time-series of the gravity current height measured at the location of the first topographic peak. In all three panels, the height of the gravity current head is comparable for $D/H = 1.0$ and $D/H = 0.75$. When $D/H = 0.5$, by contrast, the head height is notably reduced suggesting a diminished driving force. The top panel of Figure 10 indicates the maximal two-layer exchange flow solution, $h = 0.375(H - A)$, derived by Farmer and Armi.¹¹ Theory of Farmer and Armi presumes steady conditions and so is here applicable only if we examine the flow immediately behind the gravity current head. In this region, and allowing for the interfacial distortions caused by turbulent mixing, it seems likely that the exchange flow following the head is maximal when $D/H = 1.0$ and 0.75 , but not when $D/H = 0.5$. Unfortunately, it is much more difficult to determine the maximal exchange flow conditions when the ambient is comprised of two layers, rather than just one. We do not, therefore, show horizontal dashed lines in the middle or bottom panels of Figure 10 but instead refer the interested reader to Smeed.³⁸

If the conclusion to be drawn from Figures 9 and 10 is that a decrease of gravity current height results in a corresponding decrease in Fr , one might expect the front speed within a single experiment to vary as the front flows first up- then downslope over large amplitude topography. In fact, quite the opposite is true in most cases. A similar observation was made in the experimental study of Britter and Linden³² who examined downslope gravity current flow along an infinite slope. They noted that the front speed remained constant even as the gravity current head continued to increase in size due to entrainment and inflow from behind the head. Consider, for instance, Figure 11 whose CTS shows substantial variations in h/H but only modest variations in Fr (similar behavior is noted in many other experiments, both those with $\lambda = 24.0$ cm and $\lambda = 48.0$ cm). We believe that the reason for this unexpected observation is that the instantaneous front speed is influenced by the competing effects of streamline expansion/contraction and by along-slope variations of the buoyancy force. In regards to the latter, note that the direction of the vertically oriented buoyancy force varies relative to the surface tangent vector leading, in the absence of other factors, to upslope (downslope) deceleration (acceleration). On the other hand, channel depth expansion and

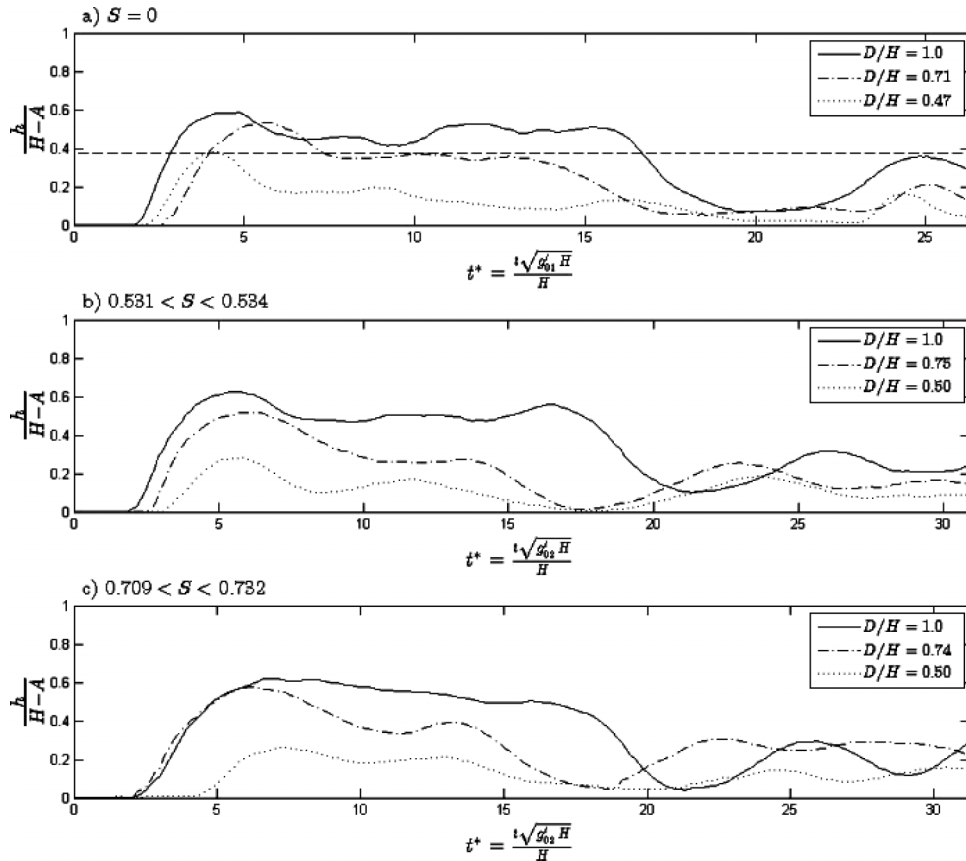


FIG. 10. Gravity current height over the first topographic peak for three different values of S and D/H . The ambient interface height is $h_1/H \approx 0.50$ for panels (b) and (c) and for all cases the topographic profile is such that $0.234 < A/H < 0.246$ and $A/\lambda = 0.167$. The horizontal dashed line in panel (a) shows the steady two-layer exchange flow solution derived by Farmer and Armi.¹¹ Note that the depressed values of $\frac{h}{H-A}$ observed at $t^* \approx 20$ for $D/H = 1$ are due to a reflected bore of ambient fluid that propagates from the lock region end-wall and whose speed is roughly proportional to $\sqrt{g'_{02} H}$. This scaling is reflected in the definition of t^* and therefore, the bore appears at approximately the same value of t^* in each of the three panels.

contraction lead, in the absence of other factors, to an acceleration of the gravity current (and the ambient return flow) as the channel depth constricts (corresponding to upslope gravity current flow) and a deceleration as the channel expands (corresponding to downslope gravity current flow). Of course, the aforementioned influences cannot be expected to counterbalance in all circumstances. Indeed, Figure 12 shows a case where $S = 0$ corresponding to a uniform density ambient; here, channel expansion/contraction seems to play the more prominent role in modulating the advance of the front, i.e., the front speed decreases on the downslope portion and increases on the upslope portion. As the inset to Figure 12 makes clear, these deceleration and acceleration correspond, respectively, to convex and concave regions in the curve describing the temporal evolution of the front.

In still other circumstances, i.e., those where A/H is large, the ambient return flow appears to be important, as, for example, in Figure 13, which shows an experiment where $A/H = 0.383$ and the ambient fluid flowing opposite the gravity current exerts a non-negligible shear stress. The ambient return flow is here important for two reasons: (i) the Reynolds number, $\text{Re} \equiv \bar{U}H/\nu$ (where $\nu = 0.01 \text{ cm}^2/\text{s}$ is the kinematic viscosity) is small, i.e., $\text{Re} = 9300$, compared to the average value of 13 800 for all full-depth lock-release experiments and (ii) as the gravity current fluid nears the top of the first peak, partial blocking occurs resulting in only a thin overflow into the following trough. The gravity current is therefore of relatively modest volume flux and inertia. As a result, much of the gravity current fluid cannot ascend the second peak and so falls backwards into the first trough

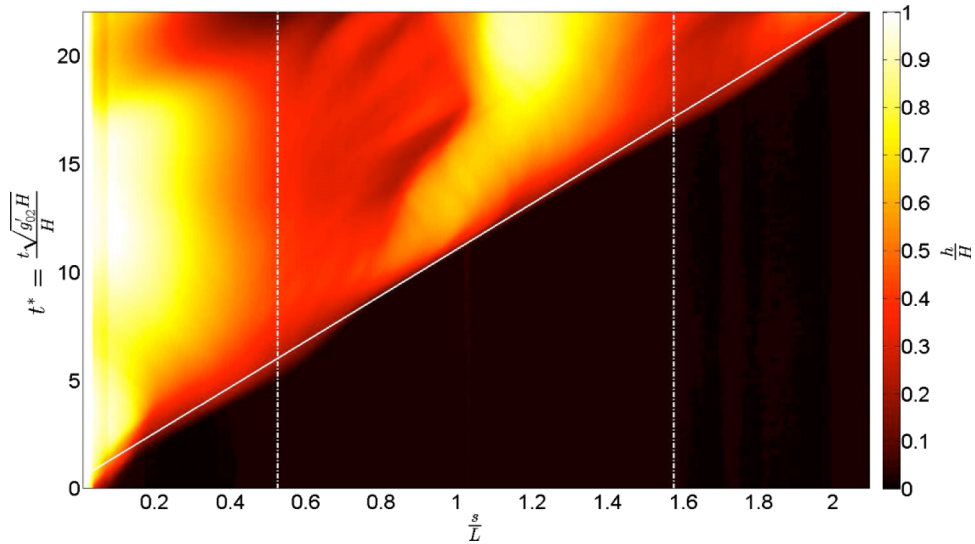


FIG. 11. CTS of an experiment where the gravity current front speed is nearly constant in spite of large variations in h/H . Experimental parameters are as follows: $S = 0.715$, $D/H = 1.0$, $A/\lambda = 0.083$, $A/H = 0.252$, and $h_1/H = 0.497$.

resulting in a sloshing-type motion of fluid of density ρ_0 . Such sloshing behaviour is examined more thoroughly in Subsection III B.

B. Motions upstream and downstream of the gravity current front

Sloshing motions behind the gravity current head were, in fact, relatively common in our experiments and were due to the formation of large Kelvin-Helmholtz vortices downstream of topographic peaks. This process is illustrated in Figure 14, which shows a jet-like flow forming on the downslope portion of the first peak leading to a region of large shear — cf. figure 2 of Gonzalez-Juez and Meiburg.³⁹ Consequently, and as anticipated by Pawlak and Armi,⁴⁰ a Kelvin-Helmholtz vortex starts to form on this downslope (or lee) side. The Kelvin-Helmholtz

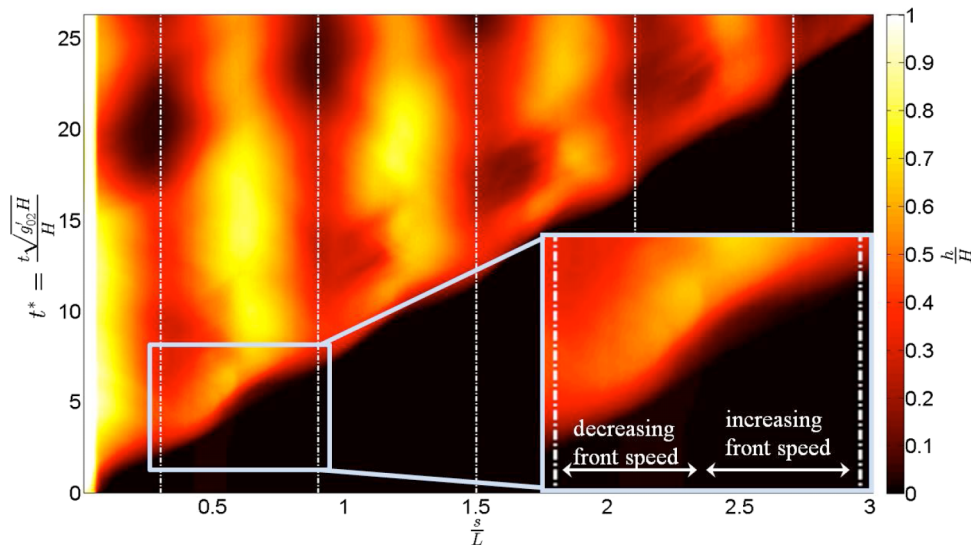


FIG. 12. CTS of an experiment where the gravity current front speed decreases (increases) on the downslope (upslope) portion of the topography. Experimental parameters are as follows: $S = 0$ (uniform density ambient), $D/H = 1.0$, $A/\lambda = 0.167$, $A/H = 0.246$.

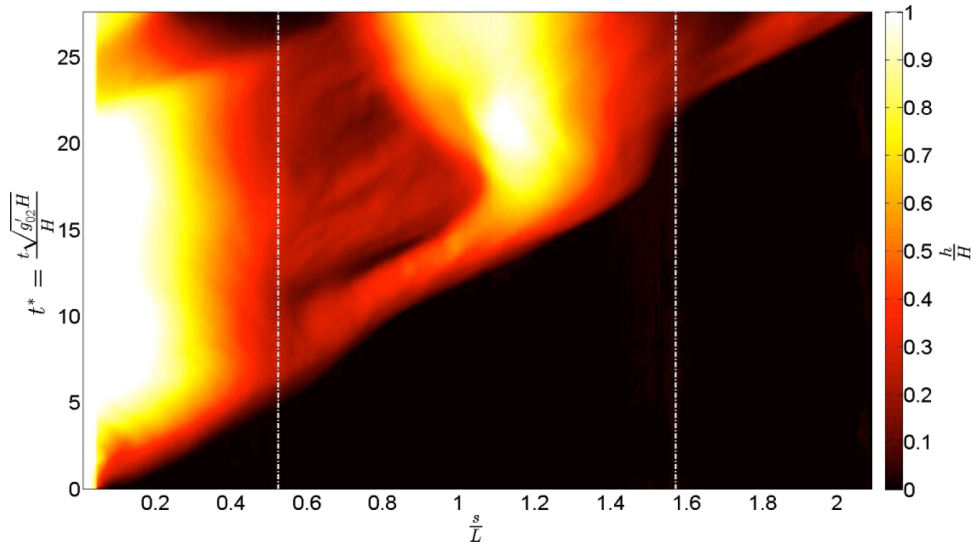


FIG. 13. CTS of an experiment where the gravity current nearly stops as a result of a strong ambient return flow at the second topographic peak. Experimental parameters are as follows: $S = 0.0938$, $D/H = 1.0$, $A/\lambda = 0.083$, $A/H = 0.383$, and $h_1/H = 0.750$.

vortex demarcates the back of the gravity current head and is apparent as the front reaches the trough. When the front propagates up and over the second peak, the Kelvin-Helmholtz vortex, described by Tokyay *et al.*¹⁹ as an “intensified mixing vortex,” reaches a maximum diameter and downstream location. It then becomes unstable in the sense that dense gravity current fluid begins to flow backwards into the trough. Thus, a sloshing mode is initiated, which in CTS images such as those of Figures 14 and 15 is characterized by sideways-V-shaped light-coloured bands—see the circled areas in the latter figure. The lower branch of the V indicates the formation, growth, and saturation of the Kelvin-Helmholtz vortex and the upper branch indicates a relaxation process that leads to dense gravity current fluid settling midway between adjacent peaks. Loosely connected with these transient events is the advection of gravity current fluid away from peaks by the ambient reflected wave. This results in peaks that are, sometimes temporarily, sometimes permanently, devoid of fluid of density ρ_0 . The process just described is evident in Figures 14 and 15 from the large dark regions centered on the vertical dashed lines for medium and/or large values of t^* .

The diameter, ℓ_0 , of the largest Kelvin-Helmholtz vortex recorded in each experiment is normalized using D similar to the process used by Özgökmen and Fischer.⁴¹ Typical ℓ_0/D values ranged from 0.1 to 0.84 and had a mean of approximately 0.44. To predict the diameter of a vortex like the one exhibited in Figure 14, we sought a correlation between ℓ_0/D and the Richardson number, Ri , where

$$Ri = g'_{10} \frac{0.4(H - A)}{(1.6\bar{U})^2}. \quad (4)$$

Here $g'_{10} = g \frac{\rho_1 - \rho_0}{\rho_0}$ is the reduced gravity based on the density difference between the gravity current and the lower ambient layer. The vertical length scale characterizing the mixing region, $0.4(H - A)$, is chosen based on empirical data from Borden and Meiburg⁴² applied to the smallest channel depth of the experiment. Finally, the velocity difference of $1.6\bar{U}$ is estimated using the theory of Farmer and Armi¹¹ assuming uniform velocities within each layer. Unfortunately, the above approach yielded results best described as mixed. In other words, and as can be confirmed from our online supplementary material,⁴³ the correlation between ℓ_0/D and Ri is less than definitive. This is not altogether surprising because Kelvin-Helmholtz vortex formation, growth, and saturation are complicated processes influenced by numerous disparate factors. Although different definitions for Ri were attempted, including ones that incorporated the upper layer density, ρ_2 , these proved no more helpful than the definition given by (4). Thus, it seems difficult to define a Richardson number

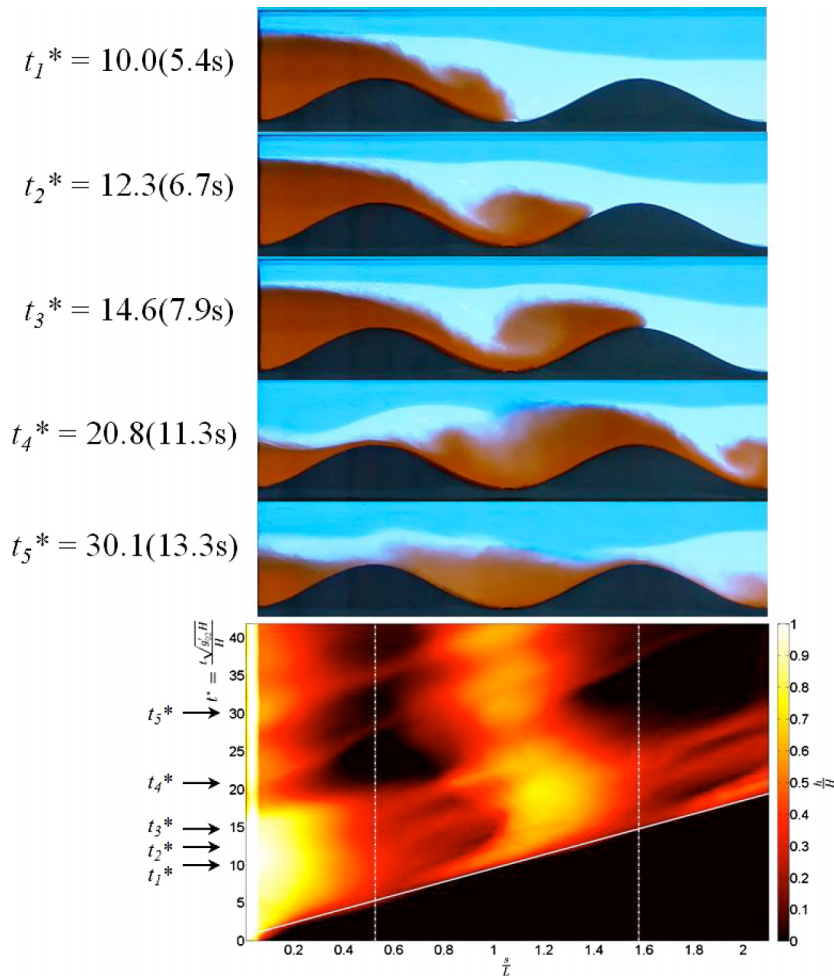


FIG. 14. Above: Experimental snapshots showing the development of a large-scale Kelvin-Helmholtz instability in the first trough. Below: the corresponding CTS. Experimental parameters are as follows: $S = 0.525$, $D/H = 1.0$, $A/\lambda = 0.083$, $A/H = 0.244$, and $h_1/H = 0.499$.

that satisfactorily encapsulates the depths and densities of all three fluid layers, at least insofar as explicating the dynamics of unsteady vortices. Further investigation of this topic is therefore deferred to future studies, the first step being to extend novel analysis of Borden and Meiburg pertaining to gravity current mixed region thicknesses to the case of flow over a non-horizontal bottom boundary.

A major focus of previous studies of gravity current flow through stratified media has been to identify parametric regime(s) where the front speed is greater than (supercritical flow) or less than (subcritical flow) the interfacial disturbance generated by the collapse and forward advance of the gravity current. For example, Tan *et al.*²⁹ found that the transition from a super- to a subcritical gravity current occurred at approximately $S = 0.75$ independent of the ambient interface height, an observation in good agreement with analytical predictions. In the present context, the job of determining whether a particular gravity current is subcritical, critical, or supercritical is made easier, if not altogether easy, using CTS images of the types shown in Figures 5 and 16. (The gravity current is respectively subcritical and approximately critical in the former and latter figures.) Because critical and supercritical gravity currents can be difficult to distinguish, we seek, for fixed topographic profile and h_1/H , the largest value of S , S_{crit} , where the flow is no longer subcritical. Results are exhibited in Figure 17, from which we conclude, consistent with Tan *et al.*,²⁹ that the interface height has a negligible influence. Thus, $S_{\text{crit}} \approx 0.75$ for $A/\lambda = 0$ (Tan *et al.*²⁹), $S_{\text{crit}} \approx 0.53$

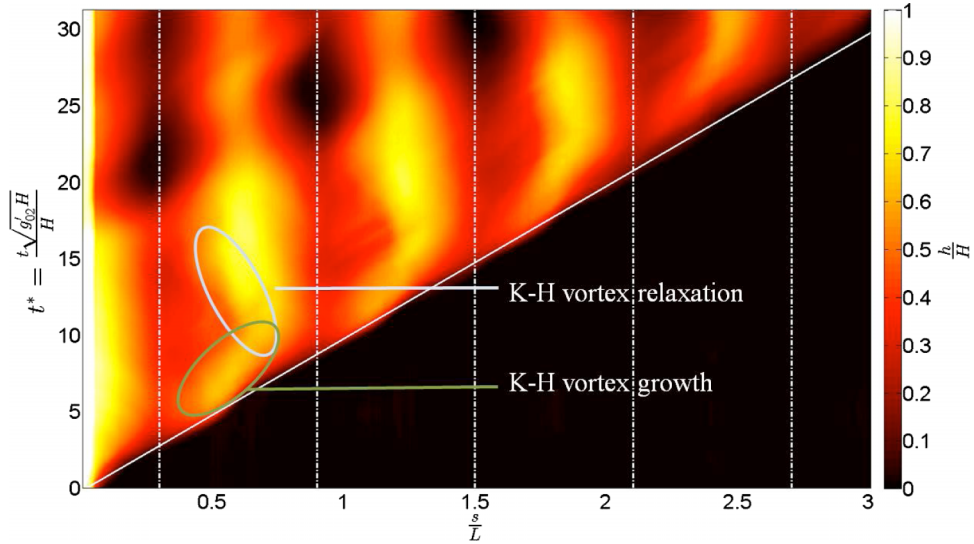


FIG. 15. CTS where gravity current fluid is initially skewed towards the downstream side of the first trough as a result of Kelvin-Helmholtz (K-H) vortex formation, growth, and saturation. As t^* increases, a relaxation occurs so that the light-coloured band settles into the middle of the trough creating a V-shape on the CTS. Experimental parameters are as follows: $S = 0.527$, $D/H = 1.0$, $A/\lambda = 0.167$, $A/H = 0.240$, and $h_1/H = 0.513$.

for $A/\lambda = 0.083$, and $S_{crit} \approx 0.37$ for $A/\lambda = 0.167$. Similar to the front speed, A/H again seems to have a very small influence on the value S_{crit} .

One reason for distinguishing between sub- and critical/supercritical gravity currents above is that the latter generally travel further faster, which is particularly important when modelling the transport of potentially hazardous material in the natural environment. Here, the situation is made more complicated by the presence of topography because tall peaks can be more effective than interfacial disturbances at arresting the gravity current front—see Figure 13, for instance. In Subsection III C, we turn finally to the topic of the downstream distance travelled by the gravity current fluid.

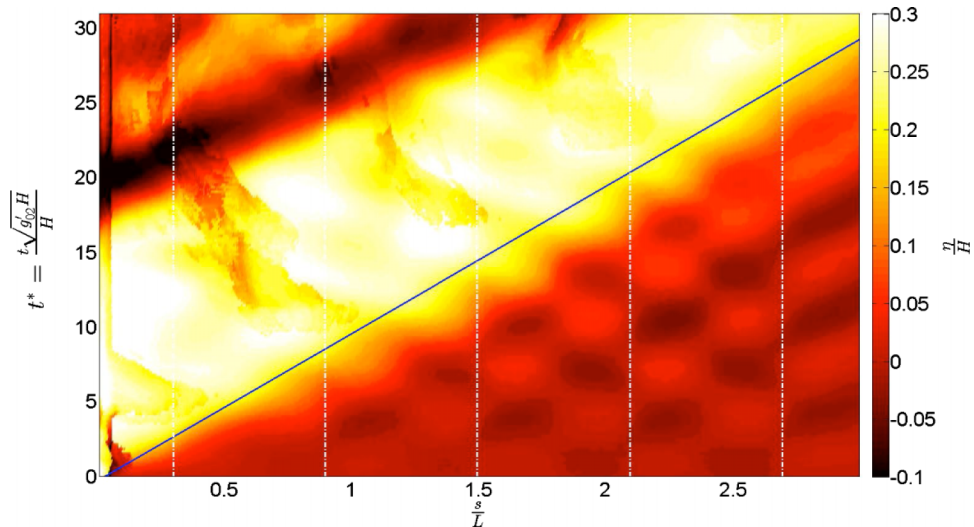


FIG. 16. CTS showing η/H for the same experiment as Figure 6. The slope of the solid line indicates the average gravity current front speed. This can be compared against the speed of the interfacial disturbance, which can be recovered from the slope of the leading edge of the light band that starts in the lower left hand corner. Here these slopes are almost equal suggesting a gravity current that is nearly critical. Ahead of the front, interfacial oscillations are present — see also Figure 5.

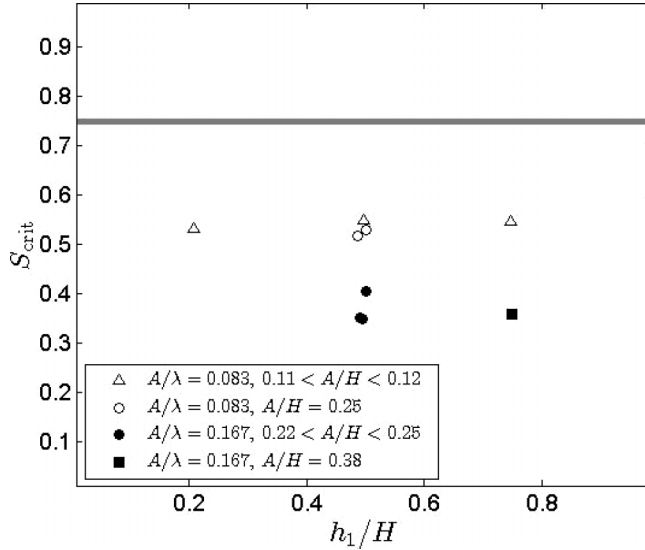


FIG. 17. The maximum value of S where the gravity current flow is not subcritical plotted against h_1/H . The thick solid line indicates the prediction from Tan *et al.*,²⁹ which applies for a horizontal bottom boundary. Note that we did not attempt to collect data when $A/\lambda = 0.167$ and $h_1/H = 0.25$ because in this case the ambient interface would fall below the topographic peaks.

C. Downstream distance traveled

One particular advantage of the partial-depth lock-release experiments is that the gravity currents have a comparatively modest volume and so do not always ascend all of the peaks comprising our topography. Thus, we can compare the downstream distance travelled by the gravity current front in the long time limit with the minimum distance predicted by a simple geometric model in which gravity current fluid is supposed to fill the bottom of the tank to a vertical distance equal to the topographic height—see Figure 18.

If mixing is neglected, the minimum number of peaks, n_{\min} , the gravity current fluid will overcome is given by

$$n_{\min} = \left\lfloor \frac{x_f}{\lambda} + \frac{1}{2} \right\rfloor \tag{5}$$

in which x_f , the horizontal distance defined in Figure 18, is determined from

$$\left(\frac{D}{H} - \frac{A}{H} \right) L = 2a \frac{A}{H} + \int_0^{x_f} \left(\frac{A}{H} \cos\left(\frac{2\pi}{\lambda}x\right) + \frac{A}{H} \right) dx. \tag{6}$$

Here a is the distance from the lock gate to the start of topography and L is the lock length. By construction, (5) and (6) are independent of S , the stratification parameter and h_1 , the ambient interface height.

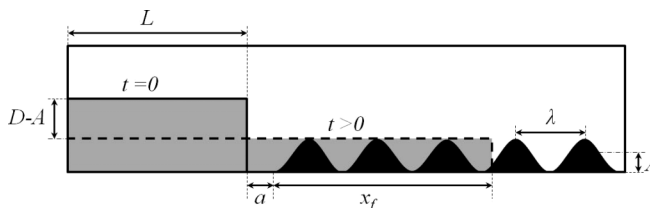


FIG. 18. Schematic showing the minimum number of peaks overcome by a (partial-depth) lock-release gravity current. For simplicity, the ambient is shown here as having a uniform density.

TABLE I. Topographic peaks overcome by the gravity current front as a function of the lock depth (D/H), lock length ($L = 48.7$ cm), and topographic profile (A/λ and A/H).

D/H	A/λ	A/H	n_{\min} from (5) and (6)	$(n_{\min})_{\text{expt}}$	$(n_{\max})_{\text{expt}}$
0.5	0.083 ($\lambda = 24.0$ cm)	0.11	7	≥ 5 [all S]	≥ 5 [all S]
0.75	0.083 ($\lambda = 24.0$ cm)	0.11	12	≥ 5 [all S]	≥ 5 [all S]
1.0	0.083 ($\lambda = 24.0$ cm)	0.11	16	≥ 5 [all S]	≥ 5 [all S]
0.5	0.167 ($\lambda = 24.0$ cm)	0.25	2	2 [$S = 0.867$]	≥ 5 [$S = 0.177$]
0.75	0.167 ($\lambda = 24.0$ cm)	0.25	4	≥ 5 [all S]	≥ 5 [all S]
1.0	0.167 ($\lambda = 24.0$ cm)	0.25	6	≥ 5 [all S]	≥ 5 [all S]
1.0	0.167 ($\lambda = 24.0$ cm)	0.39	3	4 [all S]	4 [all S]
0.5	0.083 ($\lambda = 48.0$ cm)	0.25	1	1 [$S = 0.872, 0.700$]	≥ 2 [$S < 0.700$]
0.75	0.083 ($\lambda = 48.0$ cm)	0.25	2	≥ 2 [all S]	≥ 2 [all S]
1.0	0.083 ($\lambda = 48.0$ cm)	0.25	3	≥ 2 [all S]	≥ 2 [all S]
1.0	0.083 ($\lambda = 48.0$ cm)	0.39	2	≥ 2 [all S]	≥ 2 [all S]

In some instances, particularly those with large S , the downstream flow of gravity current fluid may be temporarily arrested well before the front reaches the n_{\min} th peak, however, dense fluid continues to overflow into each trough until its supply, determined by the product of D and L , is exhausted. The final number of peaks overcome in these experiments, plus those having small or moderate S , is specified in Table I. Each row of this table considers a family of experiments having a particular combination of A , λ , D , and H but variable S in such a way that all full- and partial-depth experiments with $S > 0$ are represented in Table I. The fourth column specifies the prediction of (5) and (6) using $a = 0$. Corresponding experimental data are given in columns 5 and 6, which provide, respectively, measured values for n_{\min} and n_{\max} . Also shown are the S values corresponding to these minimum and maximum values for n . For the first and second families of experiments (corresponding to the first seven rows of the table), the topographic profile has five peaks so we report “ ≥ 5 ” for those gravity currents that overcome all five of these peaks. By contrast, there are only two peaks for the topographic profile in the third family of experiments (rows 8-11). Note that all partial-depth experiments have fixed h_1/H so we make no conclusions about the effect this ratio, which, in any event, does not appear in (5) and (6).

Of particular interest here are instances where the predicted value for n_{\min} is less than the total number of peaks; $(n_{\min})_{\text{expt}}$ is greater than or equal to n_{\min} in all such cases. When $(n_{\min})_{\text{expt}} = n_{\min}$, experiments generally exhibit minimal mixing and have a large S -value corresponding to a flow that propagates comparatively slowly downstream. Note, however, that the converse statement can be false, i.e., even when S is large, $(n_{\min})_{\text{expt}}$ may exceed n_{\min} as is the case, for instance, in the large S case from row 5. In that experiment, substantial mixing was observed to occur at early times, presumably because of the small density difference between the gravity current and lower ambient layer and in spite of the small value for Fr . Mixing by entrainment effectively increases the gravity current fluid volume above the value assumed in (6). On the other hand, there exist numerous cases that exhibit relatively little mixing but where n_{\min} is likewise exceeded, now because the gravity current has significant downstream momentum. As shown by row 8 and, more especially, row 4 of Table I, these experiments are associated with small S suggesting front speeds large enough to leave troughs under-filled with gravity current fluid in contrast to the picture suggested by Figure 18.

IV. DISCUSSION AND CONCLUSIONS

Experiments are conducted in a Boussinesq regime for high Reynolds number gravity currents issuing from either full- or partial-depth locks and flowing over sinusoidal topography below a two-layer ambient. The experimental parameters $S = (\rho_1 - \rho_2)/(\rho_0 - \rho_2)$, h_1/H , A/H , A/λ , and D/H are varied to determine the influence of the ambient density stratification, the topographic

geometry, and the initial conditions on the flow. Results are analyzed using CTS images that characterize the gravity current height and ambient interface deflection as functions of time, t , and curvilinear distance, s . From the former images, it is straightforward to evaluate the initial gravity current front speed. Front speeds are characterized in terms of a Froude number, Fr , which, consistent with the studies of Maxworthy *et al.*²¹ and Tan *et al.*,²⁹ is a decreasing function of D/H , h_1/H , and S — see Figures 7 and 9.

For fixed D/H , S , and h_1/H , the influence of the topography is to moderately depress measured values of Fr relative to the case of a horizontal bottom boundary. In this respect, the average absolute slope of the topography, A/λ , seems to exert a much more substantial influence than A/H itself — see Figure 8. Remarkably, however, local variations in the initial front speed are typically small even when the topographic amplitude is large. This is likely due to the balance of competing factors affecting the front speed, namely, a diverging/converging channel and variations of the buoyancy force as functions of s . In certain exceptional cases where A/H is large, it is possible for the front speed to be significantly retarded by the shear forces exerted by the oppositely directed ambient return flow. This adverse influence is most keenly felt in the vicinity of topographic peaks and may result in a near complete arresting of the gravity current flow — see Figure 13 and the discussion thereof.

When the gravity current is released from the lock, its collapse creates interfacial disturbances along the ambient interface. Tan *et al.*²⁹ found that, independent of the ambient interface height, the gravity current front speed approximately matches the speed of the interfacial disturbance when $S = S_{\text{crit}} \approx 0.75$ for the case of a horizontal bottom. Using data from our CTS images, we can compute the corresponding values for S_{crit} when the bottom boundary of the channel is not flat. More specifically, Figure 17 shows that $S_{\text{crit}} \approx 0.53$ when $A/\lambda = 0.083$ and $S_{\text{crit}} \approx 0.37$ when $A/\lambda = 0.167$. Consistent with investigation of Tan *et al.*, h_1/H (and also A/H) exhibit only a weak influence on measured values of S_{crit} .

Qualitatively, the gravity current structure is altered from the canonical flat-bottom case by Kelvin-Helmholtz vortices arising immediately downstream of regions of high shear. As is evident in Figure 14 most especially, these vortices create a gradient of gravity current height over a relatively limited horizontal distance. The Kelvin-Helmholtz vortices eventually relax as gravity current fluid sloshes backwards into the topographic troughs leading, in the long time limit, to a flat interface between the fluid layers having densities ρ_0 and ρ_1 .

When the gravity current has only modest horizontal momentum, which often occurs for small D and large S , the flat interface from the previous paragraph will typically coincide with the level of the topographic peaks — see Figure 18. In this case, the number, n_{min} , of peaks that a gravity current can overcome is well-approximated by the solution of (5) and (6). We often observe, however, that $(n_{\text{min}})_{\text{expt}}$ exceeds this prediction. Reasons for this disparity are twofold; mixing with the lower ambient layer effectively increases the volume of gravity current fluid assumed in (5) and (6), and the large downstream momentum possessed by gravity currents having comparatively small S .

The simple sinusoidal shape presented in this study is a starting point for future research examining how different topographic profiles can affect the propagation of a gravity current in a two-layer or continuously stratified ambient. Further to Tokyay *et al.*,¹⁹ future studies could expand upon this research by examining the influence of representative underwater bedforms in order to study oceanic flows. Alternatively, topographies could be modeled after mountainous regions in order to study atmospheric gravity currents and, e.g., their ability to bring moisture to isolated valleys. Another topic meriting additional study is to perform experiments using a one-and-a-half layer ambient, i.e., by allowing the upper layer depth to far exceed both the lower layer depth and the gravity current height (cf. Rottman and Simpson⁴⁴). In this small A/H case, the expansion/contraction of the channel is expected to be comparatively unimportant relative to s -dependent variations of the buoyancy force and thus, the gravity current front speed may exhibit greater deviations about its initial average value. Quantifying the magnitude of these deviations as a function of the relevant experimental or numerical parameters remains an open problem.

ACKNOWLEDGMENTS

Funding for this research was generously provided by the Natural Sciences and Engineering Research Council through the Discovery Grant and Research Tools and Instruments programs. Preliminary experiments of the type described in Section II were conducted by Alan Tan.

- ¹ J. E. Simpson, *Gravity Currents*, 2nd ed. (Cambridge University Press, Cambridge, England, 1997).
- ² T. B. Benjamin, "Gravity currents and related phenomena," *J. Fluid Mech.* **31**, 209–248 (1968).
- ³ I. P. Castro, W. H. Snyder, and G. L. Marsh, "Stratified flow over three-dimensional ridges," *J. Fluid Mech.* **135**, 261–282 (1983).
- ⁴ W. H. Snyder, R. S. Thompson, R. E. Eskridge, R. E. Lawson, I. P. Castro, J. T. Lee, J. C. R. Hunt, and Y. Ogawa, "The structure of strongly stratified flow over hills: Dividing-streamline concept," *J. Fluid Mech.* **152**, 249–288 (1985).
- ⁵ J. C. R. Hunt, K. J. Richards, and P. W. M. Brighton, "Stably stratified shear flow over low hills," *Q. J. R. Meteorol. Soc.* **114**, 859–886 (1988).
- ⁶ I. P. Castro and W. H. Snyder, "Upstream motions in stratified flow," *J. Fluid Mech.* **187**, 487–506 (1988).
- ⁷ I. P. Castro and W. H. Snyder, "Experiments on wave breaking in stratified flow over obstacles," *J. Fluid Mech.* **225**, 195–211 (1993).
- ⁸ P. G. Baines, *Topographic Effects in Stratified Flows* (Cambridge University Press, Cambridge, England, 1995).
- ⁹ S. E. Belcher and J. C. R. Hunt, "Turbulent flow over hills and waves," *Annu. Rev. Fluid Mech.* **30**, 507–538 (1998).
- ¹⁰ L. Armi, "The hydraulics of two flowing layers with different densities," *J. Fluid Mech.* **163**, 27–58 (1986).
- ¹¹ D. M. Farmer and L. Armi, "Maximal two-layer exchange over a sill and through the combination of a sill and contraction with barotropic flow," *J. Fluid Mech.* **164**, 53–76 (1986).
- ¹² S. B. Dalziel and G. F. Lane-Serff, "The hydraulics of doorway exchange flows," *Build. Environ.* **26**, 121–135 (1991).
- ¹³ W. D. Peters and J. E. S. Venart, "Visualization of rough-surface gravity current flows using laser-induced fluorescence," in *Proceedings of the 9th International Symposium on Flow Visualization*, edited by G. M. Carlomagno and I. Grant (Heriot-Watt University, 2000), pp. 244-1–244-11.
- ¹⁴ M. La Rocca, C. Adduce, G. Sciortino, and A. B. Pinzon, "Experimental and numerical simulation of three-dimensional gravity currents on smooth and rough bottom," *Phys. Fluids* **20**, 106603 (2008).
- ¹⁵ H. Nogueira, C. Adduce, E. Alves, and J. Franca, "Analysis of lock-exchange gravity currents over smooth and rough beds," *J. Hydraul. Res.* **51**(4), 417–431 (2013).
- ¹⁶ G. F. Lane-Serff, L. M. Beal, and T. D. Hadfield, "Gravity current flow over obstacles," *J. Fluid Mech.* **292**, 39–53 (1995).
- ¹⁷ T. M. Özgökmen, P. F. Fischer, J. Duan, and T. Iliescu, "Entrainment in bottom gravity currents over complex topography from three-dimensional nonhydrostatic simulations," *Geophys. Res. Lett.* **31**, L13212, doi:10.1029/2004GL020186 (2004).
- ¹⁸ E. Gonzalez-Juez, E. Meiburg, and G. Constantinescu, "Gravity currents impinging on bottom-mounted square cylinders: Flow fields and associated forces," *J. Fluid Mech.* **631**, 65–102 (2009).
- ¹⁹ T. Tokyay, G. Constantinescu, and E. Meiburg, "Lock-exchange gravity currents with a high volume of release propagating over a periodic array of obstacles," *J. Fluid Mech.* **672**, 570–605 (2011).
- ²⁰ T. Tokyay, G. Constantinescu, and E. Meiburg, "Lock-exchange gravity currents with a low volume of release propagating over an array of obstacles," *J. Geophys. Res.: Oceans* **119**, 2752–2768, doi:10.1002/2013JC009721 (2014).
- ²¹ T. Maxworthy, J. Leilich, J. Simpson, and E. H. Meiburg, "The propagation of a gravity current in a linearly stratified fluid," *J. Fluid Mech.* **453**, 371–394 (2002).
- ²² M. Ungarish, "On gravity currents in a linearly stratified ambient: A generalization of Benjamin's steady-state propagation results," *J. Fluid Mech.* **548**, 49–68 (2006).
- ²³ M. Ungarish, *An Introduction to Gravity Currents and Intrusions* (CRC Press, Boca Raton, FL, USA, 2009).
- ²⁴ A. W. Tan, "Gravity currents in two-layer stratified media," M.S. thesis, University of Alberta, 2010.
- ²⁵ M. R. Flynn, M. Ungarish, and A. W. Tan, "Gravity currents in a two-layer stratified ambient: The theory for the steady-state (front condition) and lock-released flows, and experimental confirmations," *Phys. Fluids* **24**, 026601 (2012).
- ²⁶ B. L. White and K. R. Helfrich, "A general description of a gravity current front propagating in a two-layer stratified fluid," *J. Fluid Mech.* **711**, 545–575 (2012).
- ²⁷ R. M. Sahuri, A. K. Kaminski, M. R. Flynn, and M. Ungarish, "Axisymmetric gravity currents in two-layer density-stratified media," *Environ. Fluid Mech.* **15**, 1035–1051 (2015).
- ²⁸ B. L. White and K. R. Helfrich, "Gravity currents and internal waves in a stratified fluid," *J. Fluid Mech.* **616**, 327–356 (2008).
- ²⁹ A. W. Tan, D. S. Nobes, B. A. Fleck, and M. R. Flynn, "Gravity currents in two-layer stratified media," *Environ. Fluid Mech.* **11**(2), 203–224 (2011).
- ³⁰ R. T. Bonnecaze and J. R. Lister, "Particle-driven gravity currents down planar slopes," *J. Fluid Mech.* **390**, 75–91 (1999).
- ³¹ L. J. Marleau, M. R. Flynn, and B. R. Sutherland, "Gravity currents propagating up a slope," *Phys. Fluids* **26**, 046605 (2014).
- ³² R. E. Britter and P. F. Linden, "The motion of the front of a gravity current travelling down an incline," *J. Fluid Mech.* **99**, 531–542 (1980).
- ³³ V. Alavian, G. H. Jirka, R. A. Denton, M. C. Johnson, and H. G. Stefan, "Density currents entering lakes and reservoirs," *J. Hydraul. Eng.* **118**, 1464–1489 (1992).
- ³⁴ J. J. Monaghan, R. A. F. Cas, A. M. Kos, and M. Hallworth, "Gravity currents descending a ramp in a stratified tank," *J. Fluid Mech.* **379**, 39–69 (1999).
- ³⁵ P. G. Baines, "Mixing in flows down gentle slopes into stratified environments," *J. Fluid Mech.* **443**, 237–270 (2001).
- ³⁶ J. W. Rottman and J. E. Simpson, "Gravity currents produced by instantaneous releases of a heavy fluid in a rectangular channel," *J. Fluid Mech.* **135**, 95–110 (1983).
- ³⁷ J. O. Shin, S. B. Dalziel, and P. F. Linden, "Gravity currents produced by lock exchange," *J. Fluid Mech.* **521**, 1–34 (2004).

- ³⁸ D. A. Smeed, "Hydraulic control of three-layer exchange flows: Application to the Bab al Mandab," *J. Phys. Oceanogr.* **30**, 2574–2588 (2000).
- ³⁹ E. Gonzalez-Juez and E. Meiburg, "Shallow-water analysis of gravity-current flows past isolated obstacles," *J. Fluid Mech.* **635**, 415–438 (2009).
- ⁴⁰ G. Pawlak and L. Armi, "Mixing and entrainment in developing stratified currents," *J. Fluid Mech.* **424**, 45–73 (2000).
- ⁴¹ T. M. Özgökmen and P. F. Fischer, "On the role of bottom roughness in overflows," *Ocean Modell.* **20**, 336–361 (2008).
- ⁴² Z. Borden and E. Meiburg, "Circulation based models for Boussinesq gravity currents," *Phys. Fluids* **25**, 101301 (2013).
- ⁴³ See supplementary material at <http://dx.doi.org/10.1063/1.4931120> for full tabulated experimental results.
- ⁴⁴ J. W. Rottman and J. E. Simpson, "The formation of internal bores in the atmosphere: A laboratory model," *Q. J. R. Meteorol. Soc.* **115**, 941–963 (1989).